Introduction, Literature Survey, Motivation & Scope of Thesis

This chapter presents introduction of hematite along with its traditional & contemporary applications. The scope of improvement in hematite properties are discussed and attempted solution methodology is described as motivation of thesis. The fundamentals of photo catalytic water splitting   (photo electrochemical property of material), radar absorbing material and uranium contamination and decontamination are described. The scope is deliberated to define the planned research work.

1.1   INTRODUCTION OF HEMATITE

The name *hematite* was originally derived from the Greek word *aematitis* means *bloodlike* about 300-315 BCE by *Theophrastus* [Rodríguez-Fernández et al., 2013]. It is not only highly abundant on earth but also on mars and responsible for its reddish color. Hematite is an iron-oxide mineral of the *Oxides & Hydroxides* group having α-Fe_2O_3 as structural formula with Trigonal crystal system. The structure of hematite is similar to that of corundum (crystalline form of aluminum oxide, Al_2O_3). It possesses rhombohedrally cenetred hexagonal structure [Yang et al., 2011].
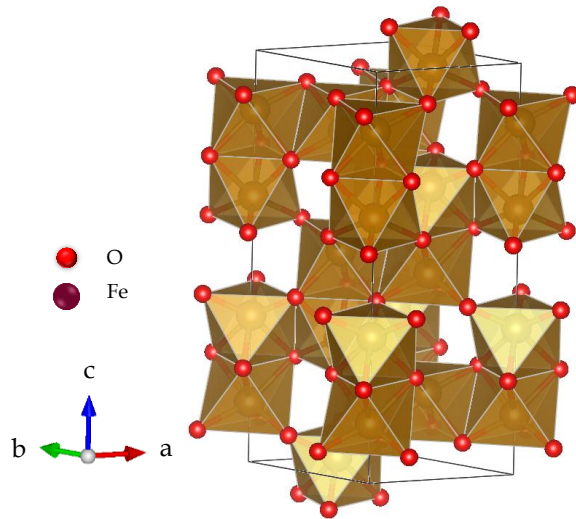

Figure 1.1: Crystal structure of Hematite (α-Fe_2O_3)

As shown in Figure 1.1, the Fe^{3+} ions are arranged in octahedral coordination with oxygen in hexagonal closest-packing (hcp anion packing). The Fe atoms occupy two out of three available octahedral sites as Fe^{3+} are trivalent ions and each of the oxygen is bonded to only two of them. This arrangement makes the structure neutral without any deficit or surplus charge. The Fe-O sheets are held together by strong covalent bonds and it results in a very hard and dense structure. The space group of hematite is R 3c (No.167, rhombohedral symmetry) [Rufus et al., 2016] .

Fe₂O₃ has many other phases like β-Fe₂O₃, ε-Fe₂O₃ and γ-Fe₂O₃ (maghemite). However, α-Fe₂O₃ is the most stable of all the phases [Machala et al., 2011]. α-Fe₂O₃ (hematite) is also known as iron^III oxide, sesquioxide, ferric oxide, iron red ochre, specular iron ore, specularite, kidney ore, martite and crocus martis. The properties of α-Fe₂O₃ are presented in Table 1.1 and are compared with other iron oxides also [Cornell and Schwertmann, 2003].

Table 1.1: General properties of Fe₂O₃ and compared with other the iron oxides

Mineral Name	α-Fe₂O₃ (hematite)	γ-Fe₂O₃ (maghemite)	Fe₃O₄(Fe^II Fe^III ₂O₄) magnetite	α -FeOOH goethite	β -FeOOH akaganite	γ -FeOOH lepidocrocite
Lattice System	Rhombo-hedral hexagonal	cubic or tetragonal	cubic	ortho-rhombic	monoclinic	ortho-rhombic
Cell dimensions (nm)	a= 0.50356 c = 13.7489	a = 0.83474	a = 0.8396	a = 0.9956 b = 0.30215 c = 0.4608	a = 1.0546 b = 0.3031 c = 1.0483	a = 0.307 b = 1.253 c = 0.388
Formula units, per unit cell, Z	6	8	8	4	8	4
Density (g cm⁻³)	5.26	4.87	5.18	4.26	-	4.09
Octahedral occupancy	$\frac{2}{3}$	-	for Fe^II 1 for Fe^III $\frac{1}{2}$	$\frac{1}{2}$	$\frac{1}{2}$	$\frac{1}{2}$
Color	red	Reddish-brown	black	yellow-brown	yellow-brown	orange
Type of magnetism	anti-ferromag. < 260 K & weakly ferromag. > 260 K	ferrimag.	ferrimag.	anti-ferromag.	anti-ferromag.	anti-ferromag.
Neel (Curie) temperature (K)	956	820-986	850	400	290	77
ΔG_f° (kJ mol⁻¹)	- 742.7	- 711.1	- 1012.6	- 488.6	-	- 477.7

α-Fe₂O₃ is the most stable form of iron oxide under ambient conditions, non-toxic with optical bandgap of 2.0-2.2 eV having n-type semiconducting properties [Hu et al., 2009]. The bulk form of hematite undergoes two types of magnetic transition. Morin transition occurs at about 260 K (T_M) and Neel transition (T_N) at about 950 K. However, nano form of hematite can show three transition temperatures i.e. blocking (T_B), Morin (T_M) and Neel (T_N) temperatures [Teja and Koh, 2009]. Hematite possesses anti-ferromagnetism with the spins lying along the electric field gradient which is oriented nearly along the *c*-crystallographic axis. At Morin transition temperature (~ 260 K) the spins are reoriented by ~90° and they lie approximately in the basal plane of α-Fe₂O₃. The adjacent spins of different magnetic sub-lattices are aligned in an almost anti-parallel manner and they are tilted (canted) by about 5°. The canted anit- parallel spin produces weak ferromagnetic moment pointing in a direction perpendicular to the basal plane. Hence, above ~260 K, hematite is believed to behave as a weak ferromagnetic or a canted anti-ferromagnetic [Anrman et al., 1965; Morin, 1950]. However, Morin transition temperature is sensitive to a number of factors including lattice defects, particle size, the presence of impurities, ion substitution, etc. [Tadic et al., 2014]. Above Neel temperature (T_N of α-Fe₂O₃ = 950 K), α-Fe₂O₃ loses its magnetic ordering and becomes paramagnet.

Each of the four different known crystalline Fe_2O_3 polymorphs has unique chemical, catalytic, magnetic, and other properties that make them suitable for specific technical applications. The α-Fe_2O_3, generally red in color, and γ-Fe_2O_3, generally red brown in color, are highly stable crystalline form and they occur in nature whereas β-Fe_2O_3 and ε-Fe_2O_3 are usually synthesized in the laboratory.

1.2 APPLICATION OF HEMATITE

The first reported use of hematite is by primitive people dating back to 40000 years for the purpose of pictograph (Figure 1.2). The application of hematite has always been multi-purpose as illustrated in Figure 1.3. Apart from bulk, nano scale hematite of various morphologies and sizes have also been synthesized and investigated.
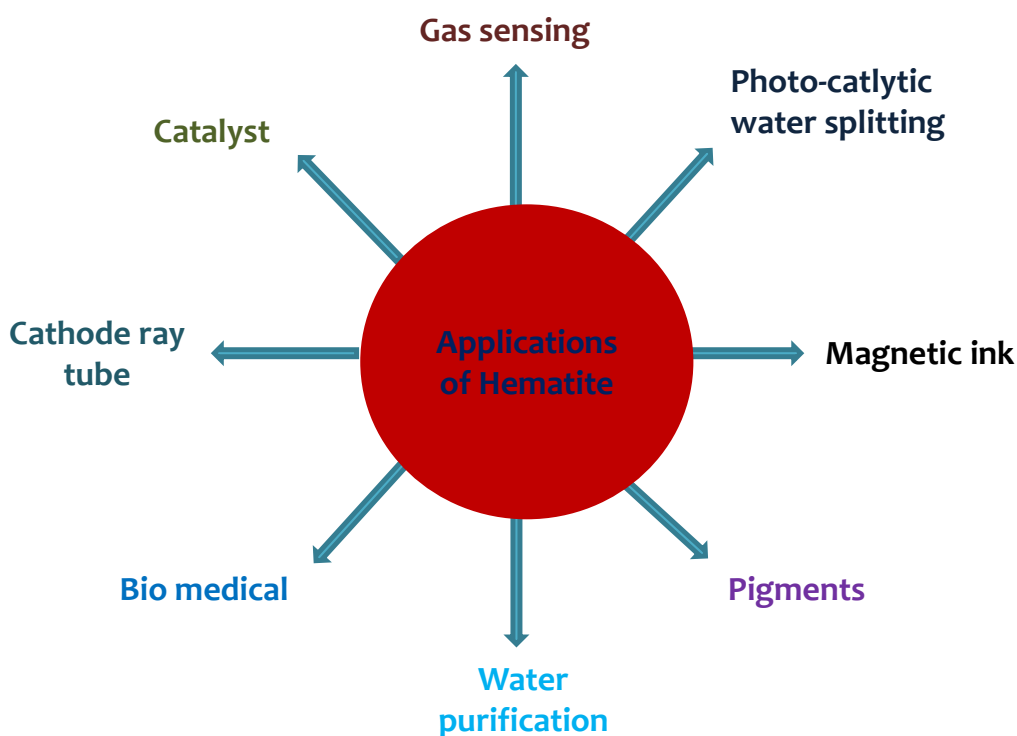

Figure 1.2: Hematite pictograph

Figure 1.3: Hematite applications/utility

The brief details on synthetic procedures, properties and applications of hematite in bulk and nano forms along with relevant references are summarized in Table 1.2.

Table 1.2: Synthesis, properties and applications studied of bulk and nano hematite

SNo	Material & Method Used	Properties/ Application	References
1.	Prepared n- type electrode of Fe_2O_3 via CVD method using iron acetyl	Photo assisted electrolysis of water	[Hardee and Bard, 1976]

	acetonate as precursor and deposited on Pt substrate at 400 °C.		
2.	High purity polycrystalline α-Fe_2O_3 and TiO_2 doped α-Fe_2O_3	Photo oxidation of water	[Kennedy and Frese, 1978]
3.	Prepared α-Fe_2O_3 from iron salts containing SO_4^{-2} ions by hydrolysis and precipitation	Gas sensing properties (H_2, CH_4, C_3H_8, C_2H_5OH)	[Nakatani and Matsuoka, 1982]
4.	α-Fe_2O_3 sol, prepared by hydrolysis at 100 °C of ferric chloride for about 24 h	Sorption of uranyl species	[Ho and Doern, 1985]
5.	CuO- Fe_2O_3 spinel structured material	Broad band electromagnetic wave absorber	[Kim et al., 1996]
6.	Natural hematite, ground to a grain size of < 100 μm	Sorption of Eu(III)	[Rabung et al., 1998]
7.	Mono disperse sol of α-Fe_2O_3 prepared by $FeCl_3$ and HCl	Sorption of Th(IV) and U(VI) in the presence of natural organic matter	[Murphy et al., 1999]
8.	Spherical α-Fe_2O_3	Uranium(VI) sorption in the presence of humic acid	[Lenhart and Honeyman, 1999]
9.	α-Fe_2O_3 collected as steel waste	Pigment	[Prim et al., 2011]
10.	α-Fe_2O_3 nanotubes prepared by thermal decomposition of $Fe(NO_3)_3.9H_2O$	Gas sensor and Lithium-ion battery applications	[Z Wang et al., 2011]
11.	α-Fe_2O_3 hollow spheres	Lithium storage	[B Wang et al., 2011]
12.	Carbon/ α-Fe_2O_3 nanocomposite	Removal of acid yellow 17 dye from water	[Ranjithkumar et al., 2014]
13.	Ni–Fe_2O_3 magnetic nanorods	Detection of uric acid	[Suresh et al., 2014]
14.	α-Fe_2O_3 coated magnetic nanoparticle	Removal of trace Sb(III) from water.	[Shan et al., 2014]
15.	Fluorine-doped α-Fe_2O_3	Hybrid super capacitor application	[Karthikeyan et al., 2014]
16.	α-Fe_2O_3 @$CoFe_2O_4$ Core-shell composites	Electromagnetic absorption	[Lv et al., 2015]
17.	α-Fe_2O_3 with different morphology	Dye-sensitized solar cells	[Shahpari et al., 2015]
18.	Biogenic hematite (α-Fe_2O_3) nanoparticles	Antibacterial and nanofluid	[Rufus et al., 2016]
19.	fluorine-doped α-Fe_2O_3 nanorods	Lithium storage	[Wang et al., 2017]

Generally speaking, hematite is a versatile material which has been studied for various applications. Hematite possesses excellent chemical and physical stability under neutral and basic conditions. In addition, hematite is cost effective and can easily be synthesized and doped in several ways. Further, it can also be synthesized on a broad range of support surfaces in different morphologies. As an example it is easy to synthesize hematite by thermal decomposition/ conversion of iron (II) and iron (III) containing compounds. Furthermore, the final product of thermally induced transformations/structural transformations of other Fe_2O_3 polymorphs also leads to formation of hematite [Darezereshki et al., 2012].

In this work, we have synthesized surface fluorinated nano crystalline hematite and explored its applications in three diverse areas namely photo electro chemical water splitting, as microwave absorbing material and uranium removal from water.

1.3   PHOTO ELECTROCHEMICAL WATER SPLITTING

1.3.1   Introduction and mechanism to water splitting

It is process of clean and renewable hydrogen production. Here, water molecules break apart into constituent hydrogen and oxygen gases using sunlight in an electrochemical system. Photons typically create electron hole pairs within the semiconductor that can react at semiconductor or electrolyte interfaces with redox chemistry [Vayssieres, 2009].
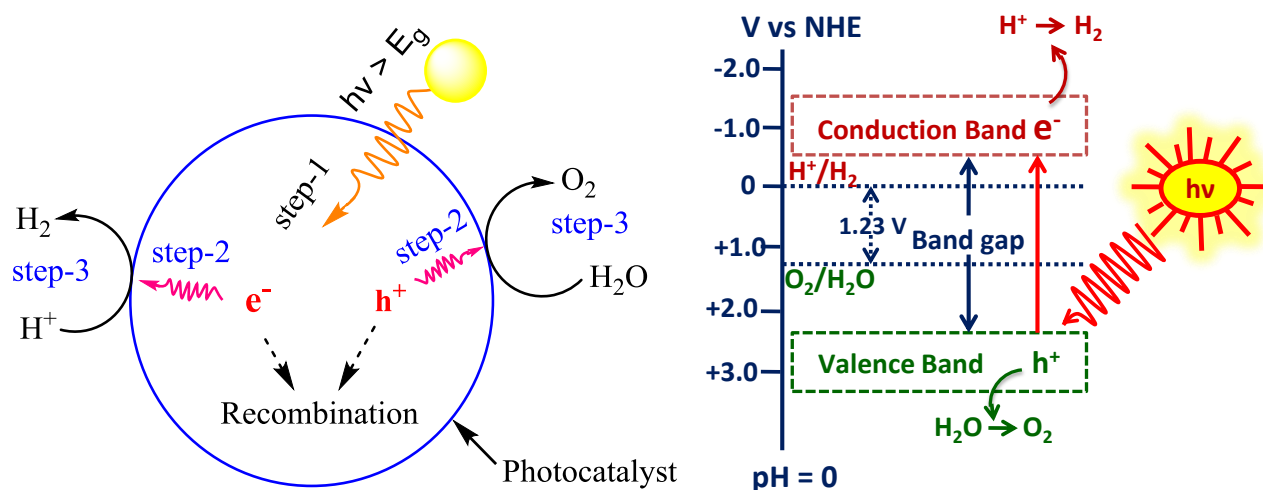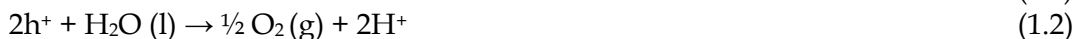

Figure 1.4: Photo electrochemical water splitting process and corresponding energy diagram

When a semiconductor electrode is illuminated with photons having an energy hv equal to or larger than the semiconductor bandgap, as presented in Figure 1.4, results into formation of electronic charge carriers, electrons in the conduction band and holes in the valence band. The PEC process is summarized in following three steps:

Step 1: Photon with energy above 1.23 eV (λ<~1000 nm) is absorbed (Figure 1.4).
Step 2: Separation of photoexcited electrons & holes and their migration to surface.
Step 3: Adsorbed species (water) is reduced by electrons and oxidized by holes.

As a consequence, oxygen is evolved at the anode and hydrogen at the cathode. The reaction mechanism can be explained in the form of two electrochemical half-reactions as presented in equation 1.3 and 1.4. Both the reactions must be sustained simultaneously, coupled by their exchange of electrons in the solid state, and ions in solution. The associated chemical reactions of complete process [Grimes et al., 2008] are presented below through equations 1.1 to 1.4:

$$2hv + Semiconductor \rightarrow 2h^+ + 2e^- \tag{1.1}$$
$$2h^+ + H_2O \ (l) \rightarrow \tfrac{1}{2} \ O_2 \ (g) + 2H^+ \tag{1.2}$$
$$2H^+ + 2e^- \rightarrow H_2 \ (g) \tag{1.3}$$
$$H_2O \ (l) + 2hv \rightarrow \ H_2 \ (g) + \tfrac{1}{2} \ O_2 \ (g) \tag{1.4}$$

Where, hv is photon energy, e^- is an electron, h^+ is a hole.

The electrons/holes are exchanged between the anode and cathode through a conductive pathway (such as a wire), and H^+ ion migration from anode to cathode through the aqueous media. As it is evident from equation 1.1 to 1.4, the PEC water splitting is a balanced chemical reaction.
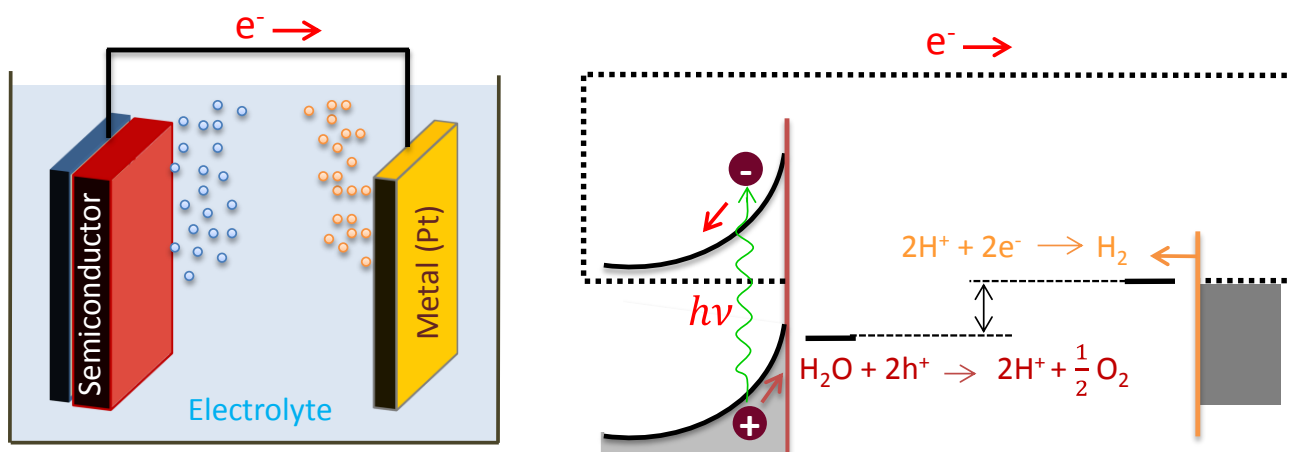
Figure 1.5: Illustration of a photoelectrochemical cell consisting of a semiconducting photoanode and platinum metal cathode. The energy diagram is shown in the right.

However, in steady-state condition the reactions in Equations 1.2 and 1.3 must be sustained at the same reaction rate. Therefore, the generation of H^+ ions (at the anode surface) and consumption (at the cathode surface) must proceed concurrently at identical rates otherwise the charge build-up will impede or even stop the entire water splitting process. The similar condition exists with the charge carriers in the solid state. The anodic half-reaction consumes two holes (supplies two electrons) and the cathode half-reaction consumes two electrons (Figure 1.5). These electrons must be transported from anode to the cathode via electrical current (such as interconnecting wire), and steady state shall be maintained only if anode and cathode reaction rates are same.

The thermodynamic parameters such as standard Gibbs free energy, standard reversible potential, described in equations 1.5 to 1.7, also plays important role in photo electrochemical water splitting.

$$\Delta G^\circ = + 237.18 \text{ kJ mol}^- \qquad (1.5)$$
$$V^\circ_{rev} = \Delta G^\circ / nF = 1.23 \text{ V} \qquad (1.6)$$
$$V_{op} = V^\circ_{rev} + Z_a + Z_c + Z_\Omega + Z_{sys} \qquad (1.7)$$

Where, ΔG° is the standard Gibbs free energy, V°_{rev} is the standard reversible potential, n is the number of electrons exchanged (02 Nos.), F is Faraday constant, V_{op} is the operational voltage, Z_a, Z_c, Z_Ω, and Z_{sys}, are over potentials associated with anode, cathode, ionic-conductivity and system losses, respectively.

The standard Gibbs free energy (ΔG°) change for splitting water into the constituent gases at standard conditions of 25 °C and 1 bar is = +237.18 kJ mol$^-$. The value of ΔG° is positive which implies that the energy needs to be supplied to drive the electrolysis process. V°_{rev} is the corresponding standard reversible potential. The minimum electrical potential needed to sustain reversible photo electrolysis is 1.23 eV. However, water splitting will not occur at a bulk potential of 1.23 V. Because the V°_{rev} value has not accounted for unavoidable process losses such as over potential loss at the anode (Z_a), over potential loss at the cathode (Z_c), ionic conductivity losses in solution (Z_Ω) and other balance-of-system losses (Z_{sys}). In real scenario, the PEC redox reactions are more complicated than the reactions described in equation 1.1 to 1.4. The water oxidation reaction at the anode is more complex and less facile, therefore, the anodic over potential losses are more severe. In addition, the electrode over potential losses of these multistep reactions, including the effects of activation energy, kinetics and mass transport can be significant, commonly several tenths of volts. Over potential losses due to ionic conductivity in the solution can also be severe. These losses depend on solution properties, as well as electrode geometry and spacing. The splitting of pure water is principally difficult due to its low conductivity ($\leq$ 0.05 Sm^{-1}) Therefore, weak acid or alkaline solutions with conductivities $\geq$ 10 Sm^{-1} are generally used. However, this creates a more corrosive environment

for the electrodes. The operating voltage (V_{op}) for water splitting must exceed V_{rev} so that it compensate for all the losses. Practically, water electrolysis systems usually require operating voltages of 1.6-1.9 V [Tuller, 2017], depending on H_2 and O_2 gas production rates.

During steady-state processes, the solid-state transporting of charges between anode and cathode represents a photon-induced current (photocurrent). It is the performance parameter of H_2 producing PEC system. Since, two electrons are consumed in the evolution of one H_2 molecule. Therefore, the rate of hydrogen production is half the rate of electron flow or half the photocurrent which can be represented as equation 1.8:

$$R_{H_2} = \frac{I_{ph}}{2e} = \frac{(J_{ph} \times Area)}{2e} \rightarrow J_{ph} = \left(\frac{R_{H_2}}{Area}\right) \times 2e \qquad (1.8)$$

Where, R_{H_2} is hydrogen production rate (s^-), I_{ph} is the photocurrent (A), e is the electronic charge (C), Area is illuminated photo electrode area, J_{ph} is photo current density (Am^{-2}).

1.3.2 Solar to hydrogen (STH) conversion efficiency

The STH conversion efficiency of solar based hydrogen production system is defined as the ratio of the useable chemical energy in the generated H_2 gas to the total solar energy supplied to the system. For steady state operations this can be written as the ratio of power output to the power input, equation 1.9:

$$\frac{P_{out}}{P_{in}} = \frac{(H_2 \ production \ rate) \times (H_2 \ energy \ density)}{solar \ flux \ integrated \ over \ illuminated \ area} \qquad (1.9)$$

Here, Gibbs energy is as the useful energy density of the hydrogen and an integrated solar flux of 1000 Wm^{-2} for AM1.5$_{global}$ solar irradiation. The STH efficiency for a PEC system can be written as shown in equation 1.10:

$$STH \ (\%) = \frac{\Delta G \ R_{H_2}}{P_{solar} \times Area} = \frac{\Delta G \left(\frac{J_{ph} \times Area}{2e}\right)}{P_{solar} \times Area} \approx 0.123 \times J_{ph} \ (Am^{-2}) = 1.23 \times J_{ph} \ (mA \ cm^{-2}) \ (1.10)$$

The first ratio in Equation 1.10 is generic for any STH production system, while the second ratio is derived specifically for PEC hydrogen evolution processes. The third term is relating conversion efficiency to the photocurrent density and it is calculated for a PEC system under AM1.5$_{global}$ solar illumination. Therefore, PEC STH efficiency is all about the photocurrent. The PEC cell should be operated at maximum photocurrent for best hydrogen-production performance. For instance, photocurrents exceeding 10mAcm^{-2} are needed for STH conversion efficiencies over 12.3%.

1.3.3 Bandgap

Bandgap is energy gap between the valence band and the conduction band electrons. The furthest band from the nucleus that has electrons in it, called the valence band (VB). The next band out to VB is called conduction band (CB).The electrons are tightly placed in VB and the electrons roam around freely in CB. Bands are the region of possible states by the law of quantum mechanics. States can be defined as probability of position of an atom which includes their energy level, momentum and spin. The bandgap of a material can be determined from a measurement of the absorption coefficient versus wavelength. The absorption coefficient can be expressed as follows (assuming the bottom of the conduction band and the top of the valence band as parabolic shape)

$$\alpha = \frac{A(h\nu - E_g)^n}{h\nu} \qquad (1.11)$$

Here, α is absorption coefficient (cm^-). A is a constant and n depends on the nature of the optical transition: $n = \frac{1}{2}$ for a direct bandgap and $n = 2$ for an indirect gap. Extrapolation of a plot of $(\alpha h\nu)^{1/2}$ versus $h\nu$ yields the indirect bandgap and a plot of $(\alpha h\nu)^2$ versus $h\nu$ gives direct bandgap of material. These plots are called Tauc plot [Tauc et al., 1966].

1.3.4 Direct and indirect bandgap

In direct bandgap semiconductor, highest point in the valence band and the lowest point of the conduction band are located at the same k-vector. Such a transition is indicated by a

vertical line in the E–k diagram and called direct transition. Here, the optical transition does not require a change in crystal momentum. In case of indirect bandgap semiconductor, the highest point in valence band and the lowest point of conduction band are located at the different k-vector [Krol and Grätzel, 2012]. Therefore, indirect transitions require change in crystal momentum ($h\omega$) as shown in Figure 1.6 and require absorption or emission of a phonon (lattice vibration) since photons carry very little momentum. The probability of occurring indirect transitions is much less and it result into much smaller absorption coefficient of indirect semiconductors as compared to direct semiconductors. The difference of absorption coefficient can be two orders of magnitude. This is why direct semiconductors can absorb much more incident light than indirect semiconductors.
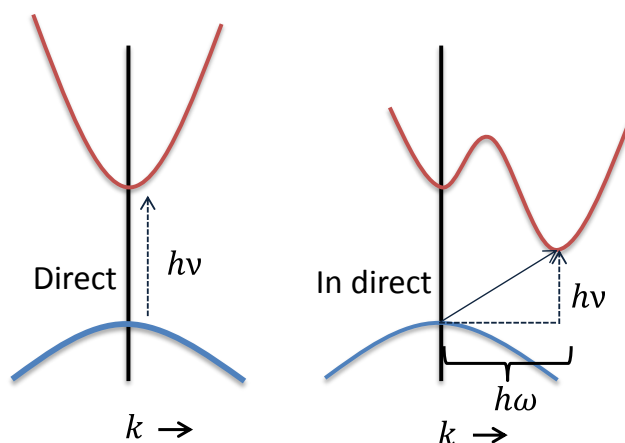
Figure 1.6: Transitions in semiconductors with a direct (left) and an indirect bandgap (right). The indirect optical transition requires assistance of phonon with energy ($h\omega$)

1.3.5   Mobility of charge carriers

It is the average velocity with which the charge carrier moves towards opposite end. The mobility of charge carrier is related to the width of the valence and conduction bands. More overlap between atomic wave functions results in broader bands and easier transport of free charge carriers through the material. The quantification can be done by curvature of the individual bands, which is directly related to the effective mass and mobility of the charge carriers. Wide bands that are strongly curved indicate high charge carrier mobility.

1.3.6   Fundamental requirements for PEC water splitting

- The essential requirement for PEC water splitting is to generate sufficient photopotential. Therefore, the bandgap energy must be large enough to overcome the reversible potential and the overpotentials needed for water-splitting. Practically, the potential should be over 1.6 eV. In simple term, there should be efficient absorption of visible light and good charge transport.
- For spontaneous water splitting process the semiconductor conduction band edge should lie at a position more negative relative to the reduction potential of water while the valence band edge more positive compared to the oxidation potential of water (NHE as reference).
- There should be sufficient photocurrent for efficient hydrogen production. In other words, semiconductor and solution properties must support the efficient generation, separation, transport and collection of photogenerated charges to drive the water-splitting reactions (in addition to the interface energetics and kinetics,).
- The catalyst must sustain over long durations with minimal corrosion and degradation.
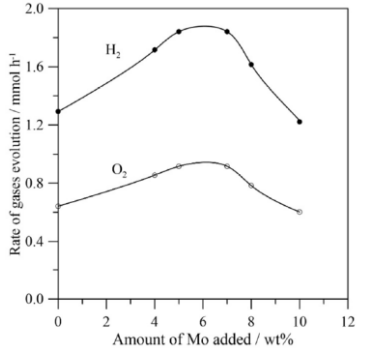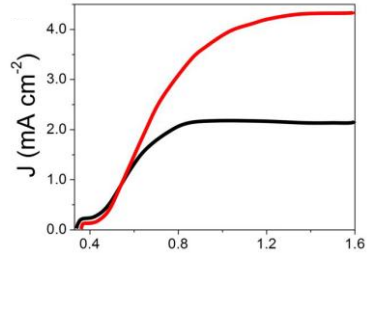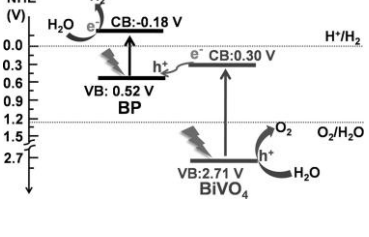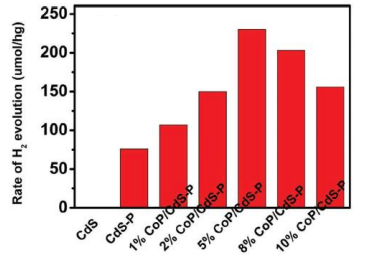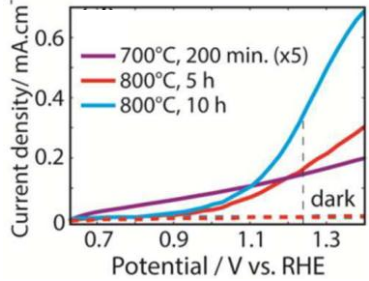- The catalyst should be cost effective for economic viability.
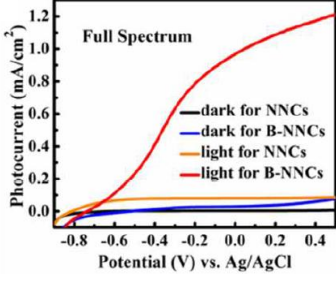
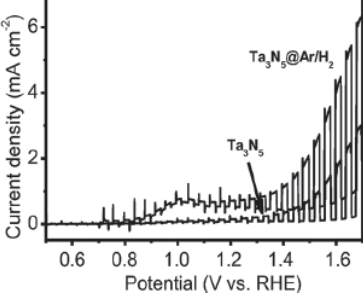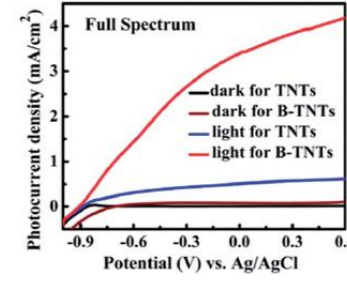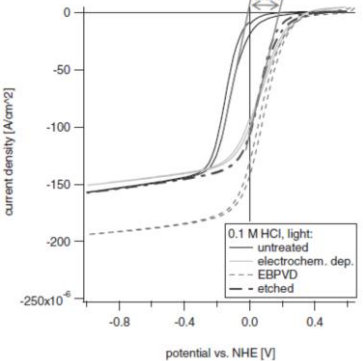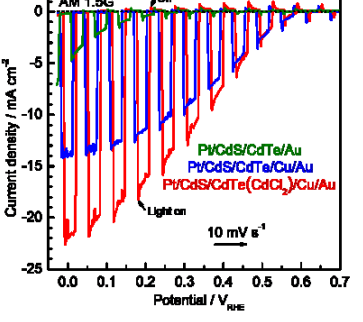### 1.3.7   PEC water splitting electrode materials

Several materials have been investigated for PEC water splitting. The literature survey
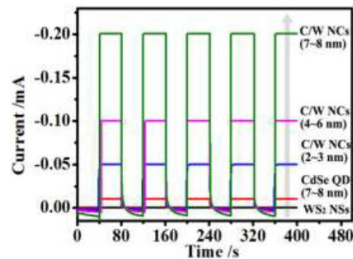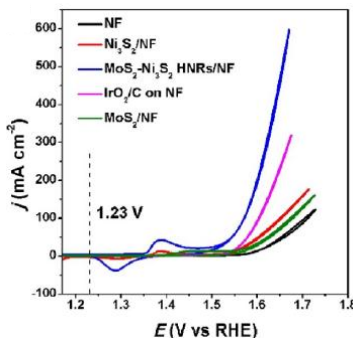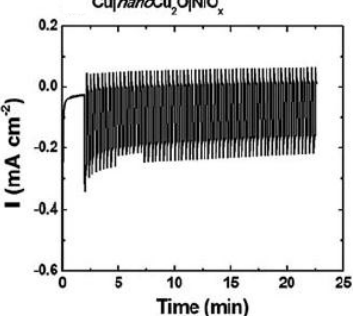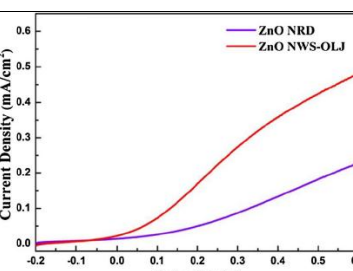
of different types of electrode material, other than hematite is present in table 1.3.

Table 1.3: Literature review of solar water splitting materials

S.No.	Material & Method	Achievement		Reference
1.	An electrochemical cell constructed using TiO_2 (1.5 mm single crystal wafer of rutile and Indium was evaporated) electrode and connected with a platinum black electrode through an external load.		First time demonstration of photoelectrochemical water splitting and achieved 1 mA cm^{-2} photocurrent.	[Fujishima and Honda, 1972]
2.	The solid-state tandem of GaAs bottom cell connected to $GaInP_2$ top cell. The $GaInP_2$ p/n junction was designed to absorb the visible portion of the solar spectrum (BG 1.83 eV) and the bottom GaAs p/n junction absorbs the near-infrared portion of the spectrum transmitted through the top junction (BG 1.42 eV).		STH efficiency was reported to 12.4%. But the employed semiconductor materials have poor stability in water (lifetime only a few hours). The cost of GaAs and $GaInP_2$ compounds are high and they are toxic as well.	[Khaselev and Turner, 1998]
3.	Dye-sensitized nanoporous TiO_2 system in which water oxidation catalyzed IrO_2 nanoparticle attached to ruthenium based dye molecule. TiO_2 and act as charge separators and the dye molecule functions as optical absorption centers.		Cost effective. However, the performance of these cells was poor (~1% quantum yield) and the dye photodegrades rapidly.	[Youngblood et al., 2009]
4.	CoO nanoparticles prepared from CoO micropowders using femtosecond laser ablation and mechanical ball milling.		Achieved overall water splitting under visible-light irradiation without any co-catalysts or sacrificial reagents. STH efficiency of around 5% was reported.	[Liao et al., 2014]

5.	Al-doped $SrTiO_3$ co-loaded with molybdenum oxide and rhodium-chromium oxide		Authors reported that 0.03 wt. % of Mo species loading enhances water splitting activity of $RhCrO_x$/STO:Al. Calcination at 573 K further improves performance. The AQY of 69% was reported at 365 nm.	[Chiang et al., 2018]
6.	Thin-layer semitransparent WO_3 electrodes. They are deposited by one-step sol-gel method on conductive oxide F-SnO_2 (FTO) substrates and annealed at higher-temperature (700 °C)		Current density was reported as 4.2 mA cm^{-2} on a 1.2-μm-thick photoanode. (2 times larger than the electrode annealed at 550 °C)	[Jelinska et al., 2018]
7.	Two-dimensional (2D) heterostructure of black phosphorus (BP)/bismuth vanadate ($BiVO_4$), an artificial Z-scheme photocatalytic system		They reported 160 and 102 $\mu molg^{-1}h^{-1}$ of H_2 and O_2 production Rates at ≥ 420 nm, without using external bias or any sacrificial agents	[Zhu et al., 2018]
8.	CoP/ interstitial P-doped CdS. Material (CdS) was synthesized by reacting $Co(OH)_2$, $Cd(OAc)_2$ and thiourea in the presence of hydrazine monohydrate.		Reported long-lived photogenerated electrons without using electron sacrificial agents. However, the reaction suffers with photocorrosion.	[Shi et al., 2018]
9.	Tantalum nitride (Ta_3N_5) and oxynitride (TaON). Nitrogen was incorporated in Ta_2O_5 films in a dry ammonia atmosphere starting at 575 °C and up to 800 °C (In-situ nitridation). Ta_2O_5 was prepared by oxidizing Ta films (prepared by DC sputtering) in tubular furnace and under oxygen flow.		They observed that the current density increases with increasing nitridation time and temperature. The efficiency is limited due to slow water oxidation kinetics. Authors further used IrO_2 to improve the IPCE.	[Dabirian and Krol, 2015]

10.	Black nanostructured niobium pentoxide (Nb_2O_5). It was prepared by anodization of Nb foil using 20 V DC power in the anhydrous glycerol electrolyte containing 10 wt. % K_2HPO_4.		They attained photocurrent of 1.02 mA cm^{-2} and applied bias photon-to-current efficiency (ABPE) of 0.345% as compared to pristine Nb_2O_5 (0.084 mA cm^{-2} photocurrent and 0.056% ABPE).	[Cui et al., 2015]
11.	Ta_3N_5 nanotube photoanodes. Ta metal was anodized under self-organizing conditions in a H_2SO_4/HF based electrolyte. The Ta_2O_5 NTs then was converted to Ta_3N_5 by a thermal treatment under Ar flow/H_2.		Ta_3N_5 NTs formed from the Ar/H_2 treated oxide show 40% increase of the photocurrent at 1.6 V_{RHE} (4.2 mA cm^{-2}) is obtained compared with the nontreated sample(1.7 mA cm^{-2}). The $Co(OH)_2$ as co-catalyst further improves the performance.	[Wang et al., 2016]
12.	Black TiO_2 nanotube arrays. Initially TiO2 nanotubes (TNTs) were prepared and further annealed at 500 °C for 4 h in air. The black TNTs were prepared by melted Al reduction of TNTs at 500 °C for 4 h.		Reported enhanced PEC water-splitting performance due to improved charge transport & separation and the extended visible light response. An applied bias photon-to-current efficiency of 1.20% was achieved.	[Cui et al., 2014]
13.	GaP semiconductor electrodes. A single crystalline wafer of GaP was cut in (100) orientation. The samples were etched with conc. HCl. Further Pt was deposited electrochemically using K_2PtCl_4 (0.5 mM) in 1 M $HClO_4$.		Untreated GaP shows a photocurrent onset at 0 V vs. NHE. After the etching in conc. HCl the onset of the photocurrent shifts 0.2 V in anodic direction.	[Ziegler et al., 2011]
14.	CdTe-based photocathodes prepared on FTO substrates. CdTe was prepared by bath deposition using 25 mM $Cd(CH_3COO)_2$, 375mM $SC(NH_2)_2$ and 14 wt. % ammonia. Further, Cu/Au back		Obtained 22 mA cm^{-2} of cathodic photocurrent density at 0 V_{RHE} under simulated sunlight. 95% incident photon-to-current conversion efficiency (IPCEs) was observed at 0 V_{RHE} at 560 and 660 nm	[Su et al., 2017]

	contact and CdCl$_2$ treatment was performed.		wavelengths.	
15.	CdSe QD/WS$_2$ Nanosheet Composite. Synthesis was carried out by wet chemical method.		They reported hydrogen evolution under visible light irradiation of 14 mmolh$^-$ and 58% quantum efficiency at wavelength λ=420 nm.	[Zhong et al., 2017]
16.	MoS$_2$–Ni$_3$S$_2$ heteronanorods supported by Ni foam. The synthesis was carried out in hydrothermal vessel.		Material displayed low η$_{10}$ values of 98 mV for HER and 249 mV for OER. A cell voltage of 1.50 V was required for 10 mA cm^{-2} current density for overall water splitting.	[Y Yang et al., 2017]
17.	Cu$_2$O|NiO$_x$ nanocomposite. The photocathode was made by annealing of Cu(OH)$_2$ nanowires on a Cu foil under N$_2$, followed by deposition of 10 nm NiO$_x$ film on the Cu$_2$O nanowires.		The Cu$_2$O|NiO$_x$ nanocomposite electrode shows a photocurrent density up to -4.98 mA cm^{-2} at -0.33 V and -0.56 mA cm^{-2} at 0.1 V versus NHE. Photostability was remained for 20 minutes.	[Lin et al., 2012]
18.	ZnO nanowires overlapping junction (ZnO NWS-OLJ) electrode prepared by solution chemical route.		The photocurrent density of ZnO NWS-OLJ electrode was reported as 57 µA cm^{-2} (2 times higher than that of the ZnO nanorods)	[Wang et al., 2019]

The prerequisites of an effective electrode materials for PEC for water splitting application includes thermal and environment stability, high quantum efficiency, durability and low cost. A survey of the various electrode materials enlisted in table reveals that the researched semiconducting electrode materials suffer from one or the other parametric drawbacks. It may be noted that no single semiconducting materials meets all the requirements. Though group III-V semiconducting materials meets all of the major requirements including high STH efficiency and optimized bandgap energies. However, their cost is high and stability is poor. On the other hand, some of the transition metal semiconductors such as TiO$_2$ and WO$_3$ are relatively environmentally and photoelectrically stable but the large bandgap energies renders them transparant to most of the incident solar radiation thereby limiting their overall photoconversion efficiency. Figure 1.7 give a comparative values of photocurrent with respect to bandgap energies of some of the transition metal semiconducting materials based PEC devices.
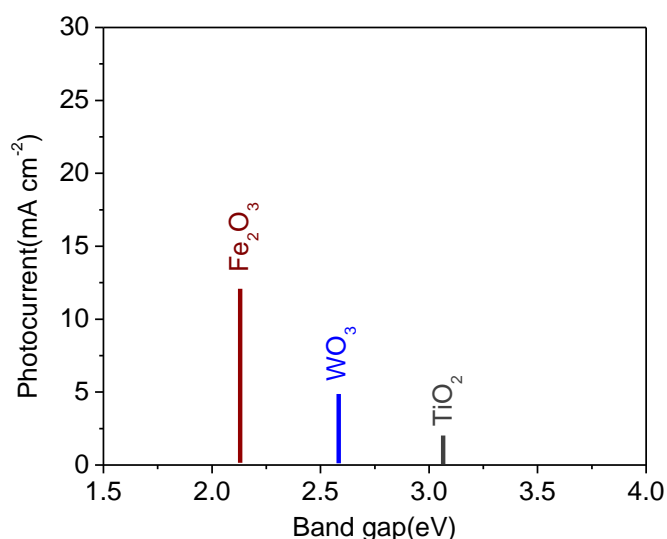
Figure 1.7: Maximum attainable AM$_{1.5\ global}$ photocurrent densities (mAcm^{-2}) for single junction PEC devices shown as a function of semiconductor bandgap

1.3.8   Hematite for PEC water splitting

It is apparent from figure 1.7 that iron III oxide may be a potential material for water splitting of PEC devices. It has been reported to have a potential of converting 12.9% of solar energy into hydrogen [Murphy et al., 2006] due to its bandgap energy of around 2.2 eV covering good portion of energy of the visible light. Further, iron oxide is also nontoxic and low cost material among various   phases of iron oxide the α form is mostly studied material for hydrogen production owing to its ease of synthesis together with excellent chemical stability and structural integrity.
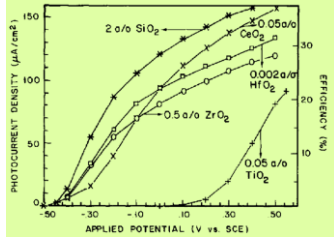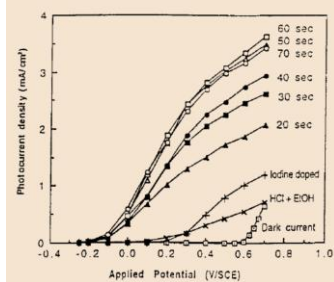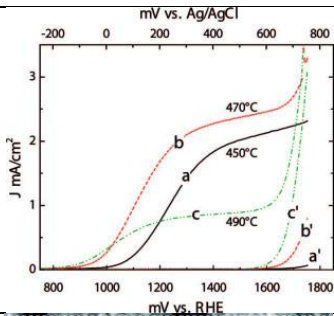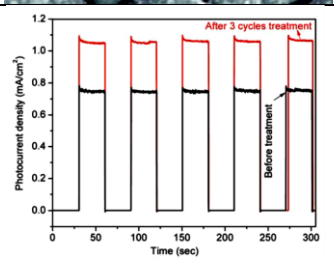
Though α-Fe$_2$O$_3$ is advantageous in many respect however, some of the following given shortcomings are needed to be addressed before making it a material of choice for PEC water splitting applications.
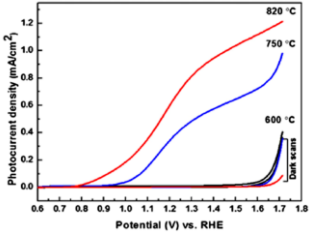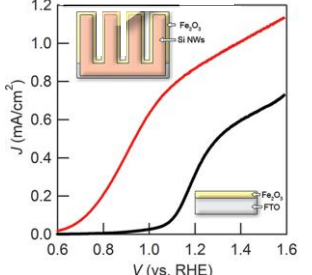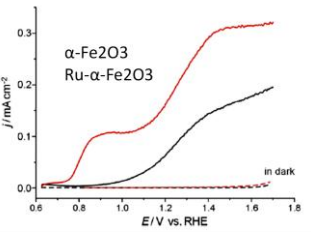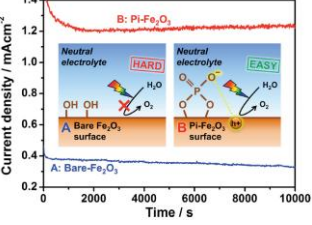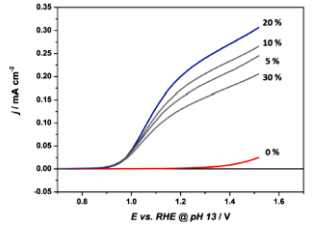
- Position of conduction band edge is at 0.21 V versus normal hydrogen electrode [Butler and Ginley, 1978]. Therefore, there is mismatch of hematite's conduction edge position and the energy levels of water reduction (0.0 V versus NHE). A necessary reduction potential is required at the counter electrode for water splitting.
- Low mobility of carriers (< 0.1 cm^{2}V^{-1}s^{-1}) [Morin, 1954]
- Hematite has high recombination rate of electron and hole
- Short diffusion length (2–4 nm) [Morin, 1954] and short excited state lifetime (< 10 ps) [Cherepy et al., 1998].
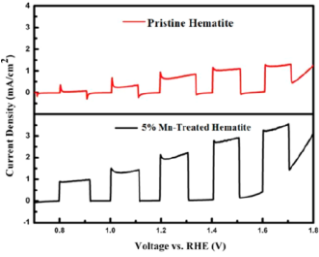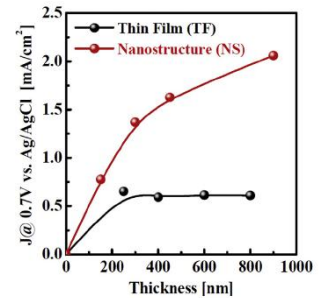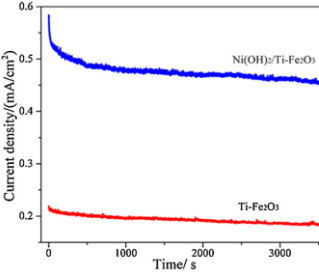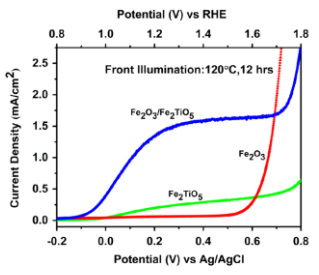
To address the above mentioned shortcomings with hematite, researchers have tried several methodologies such as forming multi quantum system, employing nano material to circumvent short hole diffusion length, improved synthesis method to address low mobility, doping to improve conductivity etc. A literature survey in this regard consisting of different synthetic methods of photoanode material and achievements are summarized in table 1.4

Table 1.4: Literature survey of hematite as photo anode material

S.No	Material & Method	Achievement		Reference
1.	Hematite and TiO$_2$ doped hematite. α-Fe$_2$O$_3$ electrode was made by ultrapure material which was pressed and sintered in air from 1050 °C to 1320 °C for 4 hr. and then		First study of hematite as photoanode. The effects of electrolyte on measured photocurrent efficiencies studied. Donor densities and flat band potentials for the	[Kennedy and Frese, 1978]

	quenched in room temperature air. The TiO_2 doping level was varied from 0.05% to 2%.		polycrystalline α-Fe_2O_3 measured.	
2.	α-Fe_2O_3 doped with CeO_2, V_2O_5, HfO_2, Nb_2O_5, WO_3, Ta_2O_5, Fe_3O_4, FeO, Al_2O_3, & Al_4C_3. The material was pressed in pellets and sintered in air at 1000-1375 °C. Doping level was kept from 0.01 to 2.0%.		It was found that dopant with oxidation state +4 to +6 are effective for α-Fe_2O_3 photoanodes. The doping levels vary for each dopant for best results and were not always the lowest doping levels.	[Shinar and Kennedy, 1982]
3.	n-Fe_2O_3 photoanode. Thin film of material was coated on SnO_2 glass sheet by spray pyrolysis method.		PEC water splitting was found to depend on the spray time, solvent composition, substrate temp., and the conc. of the spray solution. The maximum photocurrent density of 3.7 mA cm^{-2} was obtained at 0.7 V_{SCE}.	[Khan and Akikusa, 1999]
4.	Silicon nanostructured hematite photoanodes. Mesoporous films of hematite were grown on SnO_2:F (FTO) from the APCVD of precursors tetraethoxysilane (TEOS) and $Fe(CO)_5$.		Effect of annealing temperature, thickness of film and silicon doping on the performance of solar water splitting studied.	[Cesar et al., 2009]
5.	Nanostructured host scaffold of WO_3, supporting a thin layer of hematite nanoparticles. The thin film was deposited by APCVD.		Host-guest electrodes reported 20% increase in the photocurrent as compared to the same quantity of hematite without the host scaffold.	[Sivula et al., 2009]
6.	ZnO over layer on the top of α-Fe_2O_3 thin film. The α-Fe_2O_3 photoanodes were fabricated by spray pyrolysis. Surface treatment was done by spin-coating of 25 mM zinc acetate solution in C_2H_5OH and further annealing at 400 °C for 20 min.		The photocurrent increased to 1.08 mA cm^{-2} (> 40%) at 0.23 V vs. Ag/AgCl and onset potential for water oxidation shifted by -170 mV. It was attributed to reduction in surface defect and changes in flat band potential.	[Xi et al., 2012]

7.	Nanostructured α-Fe_2O_3 thin film. It was deposited over FTO using three electrode system and an aqueous solution of 0.05 M $Fe(NH_4)_2(SO_4)_2$.$6H_2O$, 0.05 M anhydrous Na_2SO_4 and 0.02 M sodium acetate trihydrate. The electrochemically grown FeOOH films further annealed to get hematite film.		Authors reported the maximum photocurrent density of 0.67 mA/cm^{-2} at 1.23 V and 1.0 mA/cm^{-2} at 1.55 V versus RHE under AM 1.5 G 100 mW/cm^{-2}. The onset water photooxidation potential of 0.8 V was reported for the electrode.	[Rahman and Joo, 2012]
8.	Hematite/Si Nanowire. hematite was grown on vertically aligned silicon nanowires (NWs) using atomic layer deposition (ALD) to form a dual-absorber system.		They reported 0.6 V_{RHE} photocurrent onset potential. It was found promising to directly couple small bandgap material with hematite.	[Mayer et al., 2012]
9.	α-Fe_2O_3 and molecular Ru catalyst. The Ru complex was loaded onto the α-Fe_2O_3 electrode by self-assembly and by drop casting. The hematite photoanode was prepared over FTO by hydrothermal method.		The photocurrent increases by nearly 50% at 1.23 V (vs. RHE). The increase in photoanode efficiency was ascribed to the heterojunction effect and catalytic effect.	[Chen et al., 2013]
10.	Phosphate deposited α-Fe_2O_3. Hematite film was grown over FTO in hydrothermal vessel using 0.15 M $FeCl_3$·$6H_2O$. The hematite photoanodes were prepared by annealing at 800 °C. Surface phosphate ion deposition was carried out by immersion in 0.5 M Na_2PO_4 for 1 h.		Phosphate deposited α-Fe_2O_3 shown improved current density 1.2 mAcm^{-2} as compared to bare α-Fe_2O_3 and it was due to phosphate group interaction with holes formed in the bulk hematite.	[Kim et al., 2014]
11.	Sn doped α-Fe_2O_3. The preparation was carried out by adding $Sn(OAc)_4$ solution to 1.56 mM $Fe(NO_3)_3$.$9H_2O$ and block copolymer Pluronic P123 0.25 g solution in 10 mL tert-butanol. The solution was further sonicated.		20% Sn surface doping exhibited maximum current density. IMPS shows increment in hole transfer rate by 10 fold compared to bare α-Fe_2O_3.	[Dunn et al., 2014]

12.	Mn doped hematite. α-Fe_2O_3 nanorods were grown on FTO by a hydrothermal method in the presence on $MnCl_2 \cdot 4H_2O$ (1-10%).		5 mol % Mn treatment showed a photocurrent density of 1.6 mAcm^{-2} at 1.23 V versus RHE (75% higher than that of pristine hematite) and of 3.2 mA cm^{-2} at 1.8 V versus RHE in a 1 M NaOH electrolyte solution (pH 13.6).	[Gurudayal et al., 2014]
13.	Nanostructured Ti-α-Fe_2O_3. The material was prepared by mixing α-Fe_2O_3 and TiO_2 in a ball-mill with ZrO_2 balls for 24 h and then dried, granulated, pressed and sintered at 900 °C for 12 h.		The photocurrent density of 2.1 mAcm^{-2} (versus Ag/AgCl) was obtained from the 1.0 at% Ti-doping. It was 220% higher than α-Fe_2O_3 thin film due to improved charge collection.	[MH Lee et al., 2014]
14.	$Ni(OH)_2$/Ti-Fe_2O_3 photoanode. Ti-Fe_2O_3 was synthesized in auto clave using $FeCl_3.6H_2O$, Na_2SO_4 and TiF_4 powder. The prepared Ti-Fe_2O_3 was treated in 20 mL of 0.05, 0.1, 0.2 and 0.4 molar $Ni(NO_3)_2$ at 85 °C for 5 h.		Photocurrent density of 0.39 mAcm^{-2} at 1.23 V_{RHE} was achieved. The performance of Ti-Fe_2O_3 was improved upon $Ni(OH)_2$ loading via reducing overpotential of OER and the recombination rate of the charge carriers.	[Li et al., 2015]
15.	Crystalline Fe_2O_3/Fe_2TiO_5 heterojunction nanorods. Material was deposited on FTO substrate by initially fabricating hematite nanorods and subsequently pseudobrookite (Fe_2TiO_5) nanoporous thin film on top of hematite film.		Surface charge separation efficiency of 85% and photocurrent density of 1.4 mAcm^{-2} at operating voltage of 1.23 V vs. RHE was achieved due to favorable band alignment & enhanced charge separation.	[Bassi et al., 2016]

1.4 RADAR ABSORPTION

1.4.1 Introduction

Radar is the acronym of radiation detection and ranging. It is one of the most versatile equipment used in detection and control of movements of flying objects. It mostly works on microwave frequencies. Basically it is an active detection device working at microwave frequencies which is widely used in detecting enemy's combat aircrafts. For military technologies, it is great concern to avoid detection of its combat aircraft from the evil radar eyes of the adversaries to be attacked. The technology to do so is known as stealth technology which can be achieved by designing aircrafts in such a way so that to deflect away incident electromagnetic radiation thrown by radar and or modified structured material of the target which can absorb the incident radiation. Such materials are known as radar absorbing (RAM) or stealth material. RAM materials have studied for their key role in imparting stealth features to

various combat military targets such as fighter aircrafts, ships, tanks, etc. [Micheli et al., 2014; Ohlan et al., 2010]. They are a special class of material that converts radar (electromagnetic) energy to some other form of energy (e.g. heat).

There are three major categories of RAM material namely: resistive-type, dielectric- type, and magnetic-type [Yuping Duan, 2017]. In resistive type materials, such as carbon black (CB), metal powders, and silicon carbide, microwave absorption depend on its conductance and permittivity. In dielectric-type materials such as barium titanate and ferroelectric ceramics EM waves is mainly absorbed through the dielectric polarization relaxation. In magnetic-type materials such as ferrite and carbonyl-iron, microwave absorption occur mainly from resonance and hysteresis losses [Pourabdollahi and Zarei, 2017]. In addition, MW absorption can also take place from plasma created around the target. Besides high absorption over broad frequency, the other important characteristics of an ideal RAM include their low density, low cost, high stability and integrity over a broad temperature range [Vinoy and Jha, 1995].

1.4.2   Literature survey of radar absorbing material in the context of iron and iron oxide

Among the magnetic RAMS, spinal and hexagonal ferrites and carbonyl iron (CI) are widely studied because of their excellent soft magnetic properties such as high saturation magnetization and high permeability [Han et al., 2012; Wei et al., 2010]. CI contains fine iron particles obtained by decomposition of iron carbonyl in an inert atmosphere. Feng *et al*. reported reflection loss < - 13 dB over the range of 6–18 GHz and reflection loss < - 8 dB over the range of 2-18 GHz using carbonyl iron and barium ferrite, respectively [Feng et al., 2007]. Meshram et al. developed hexagonal ferrite powder showing minimum absorption of 8 dB from 8 to 12 GHz [Meshram et al., 2004]. Rana *et al*. investigated cobalt substituted M-type barium ferrite for RAM in Ku-band (12–18 GHz) [Rana et al., 2018]. In addition to this, iron oxide materials are also studied for RAM application. Wang *et al.* have synthesized polyaniline/γ-Fe_2O_3 nanocomposite and reported its MW absorption in the range of 13.4 and 16 GHz [Wang et al., 2008]. Sun *et al.* reported microwave absorption of iron nano particles at microwave frequencies particles in the range of 2-9 GHz by reduction of Fe_3O_4, γ-Fe_2O_3 by a reduction-oxidation process from dendritic α-Fe_2O_3 and found them as potential microwave absorber in the range of 2-9 GHz [Sun et al., 2011].

As such, Hematite (α-Fe_2O_3) is the most thermodynamically stable phase of iron oxide together with nontoxic having high resistance to corrosion. It has been extensively investigated for a variety of applications such as photo catalysis, water treatment, and electrode in lithium batteries, production of magnetic materials, electromagnetic devices, paints and pigments. However, it shows poor microwave absorption characteristics due to nonmagnetic nature [Brezesinski et al., 2006]. Interestingly we have observed the enhancement in magnetism in surface fluorinated α-Fe_2O_3. It has motivated us to study its microwave absorption characteristics over a broad frequency range (5-18 GHz).

1.5   URANIUM REMOVAL FROM WASTE WATER

Uranium occurs naturally in the earth's crust and surface & ground waters in soluble form mostly near Uranium mines. U(VI) is released into the environment through several sources, such as natural deposits, nuclear industries, fertilizers and other processing of uranium application. Chronic exposure of uranium radionuclide in waste water is a potential health hazard [Komulainen et al., 2010]. Accumulated uranium in human body results in chemical and radioactive effects. The major sites of uranium deposition in the body are the kidneys, liver and bones. As per World Health Organization, the provisional guideline value for total content of uranium in drinking-water is 30 μgL^{-1} based on its chemical toxicity [WHO, 2011]. U(VI) is released into the environment through several sources, such as natural deposits, nuclear industries, fertilizers and other processing of uranium application. A number of conventional methods for the removal of uranium ions from aqueous solutions have been used.

1.5.1 Literature survey of uranium removal methodologies

The literature survey of different methods for treating uranium contaminated water and or uranium extraction is summarized in table 1.5.

Table: 1.5: Uranium removal/extraction methodologies

S.No.	Process	Comments	Reference
1.	Chemical precipitation	It uses flocculants (such as CaO and $Mg(OH)_2$ etc.), coagulant aid (such as clay, activated SiO_2 and polymeric electrolytes, etc.) for uranium precipitation.	[IAEA, 1992]
2.	Solvent extraction	Uranium extracted using organic solvents. The most well-known process worldwide for extraction of uranium is the Plutonium Uranium Redox Extraction (PUREX) process, where nitric acid solution (extractant) is used with Tributyl phosphate (TBP).	[Mathuthu et al., 2019]
3.	Membrane separation	Nano filtration and reverse osmosis are used for separation of uranium binary system and concentrate uranium from drinking water respectively.	[Figoli et al., 2016; Ghasemi Torkabad et al., 2017]
4.	Ion exchange	The sorption of ions by ion-exchangers takes place by exchanging counter ion at ion exchanger surface (in-organic and organic). Inorganic ion-exchangers e.g. zeolites and clays are generally of higher chemical, radiolytic & thermal stability. They are also cost effective as compared to the organic resins. However, the inorganic exchangers absorb uranyl ion (UO_2^{+2}) only within a very narrow pH range of 4-7.	[Manos and Kanatzidis, 2012]
5.	Electrochemical	Voltages applied to electrode to attract the ions and induce electrodeposition of UO_2^{+2} ions to form charge-neutral uranium species. Functionalized electrodes offer surface specific binding to uranyl ions.	[Chi et al., 2018]
6.	Cementation	Cementation is used to transform waste into a stable solid form that is insoluble and will prevent spreading to the surrounding environment.	[Osmanlioglu, 2002]
7.	Evaporation	It leads to decontamination factors in the range $10^4 - 10^6$. The main difficulties encountered in evaporation are high cost, foaming, crust formation and evaporation of volatile compounds.	[Duff et al., 1997]
8.	Bio-sorption	Biomass of living and non-living algae (Sargassum & Chlorella), fungi, yeast, bacteria, actinomycetes, reported for sequestering uranyl ions from aqueous solution.	[KY Lee et al., 2014; Yang and Volesky, 1999]
9.	Adsorption on various adsorbents	Adsorption takes place by physical forces (physisorption) at the surface of adsorbent. It is easy to operate, generates low waste and cost effective.	[Gao et al., 2014; Kausar and Bhatti, 2013],

Most of the methods as mentioned in table 1.5 have some limitations such as high cost, low efficiency, toxic waste production and high energy consumption. Among the various removal methodologies for uranium (VI), adsorption is the most practiced technique due to its ease of operation, considerably low recurring cost and low waste generation. Several adsorbents including nano materials and activated carbon have been reported and enumerated table 1.6.

Table: 1.6: Literature survey of adsorbents used for uranium removal from water

| S.No.	Material and Method	Comments	Reference
1.	Activated carbon fibers anchored on salophen (ACF-Sal).	The maximum uranium (VI) adsorption capacities of ACF-Sal was found to be 142.8 mg g^{-1} at pH 6	[Mishra et al., 2015]
2.	Polyethyleneimine modified activated carbon studied in batch method.	The adsorption capacity of sorbent for U(VI) was estimated to be 115.31 mg g^{-1}	[Saleh et al., 2017]
3.	Silicon dioxide nanopowder. Adsorption studies were carried out in batch and fixed bed column.	At pH 5, the maximum adsorption capacity (q$_{e, max}$) was attained as 59.92 mg g^{-1}.	[Mahmoud, 2018]
4.	Titanium dioxide (98% TiO2 was rutile and ~2% anatase).	The adsorption density of uranium (VI) on TiO$_2$ reaches its maximum at low pH (3 to 5)	[Lamb et al., 2016]
5.	Alumina. The alumina hollow microspheres were prepared in HT vessel using aluminum isopropoxide	The materials exhibited adsorption capacity of 34.9 mg g^{-1} calculated from the Langmuir model for the removal of uranium (VI) from aqueous solution. The optimum pH was 5.	[Yu et al., 2013]
6.	Carbon nanotubes. Adsorption capacity was deduced using batch experiments.	The U(VI) adsorption onto CNTs reached equilibrium within 10 min. and the removal efficiency was 95% at pH = 5. The q$_{e, max}$ was 10.71 mg g^{-1}.	[Yu and Wang, 2016]
7.	Bentonite activated clay. The clay was treated with 4% NaCl solution followed by HCl treatment.	85% uranium removal efficiency was obtained at pH 4. The adsorbent capacity was estimated to 11.8 mg g^{-1}.	[W Youssef, 2017]
8.	Fe$_3$O$_4$ magnetic nanoparticles. 18-crown-6 was grafted to the magnetic particles to form the second surface coating.	The maximum uranium (VI) sorption capacity was 91.12 mg g^{-1} at 45 °C, pH 5.5 for 30 min.	[Li et al., 2013]
9.	Zirconyl-molybdopyro phosphate tributylphosphate (ZMPP-TBP) prepared by co-precipitation method.	A maximum removal of 99.31% and capacity of 196.08 mg g^{-1} were achieved at pH 6.0.	[S Zhou et al., 2013]
10.	Zeolite composite, obtained from coal fly ash and magnetite	The adsorption capacity was estimated to 22.4 mg g^{-1} using Langmuir model. The pseudo- second-order kinetics model was used for describing the adsorption process.	[Fungaro et al., 2012]

Therefore, several materials have been tried for uranium removal from contaminated waste water. However, cost effective and efficient remediation technology is required to tackle the removal of uranium from large quantity of wastewater. Iron is an abundant element in earth crust and iron oxides are extensively distributed in the environment. Iron oxides, particularly α-Fe$_2$O$_3$ are common components of soil and sediment. They are a relatively cost effective material compared with other adsorbents. The α-Fe$_2$O$_3$, which has a large specific surface area and high adsorption capacity are of specific interest for waste water treatment applications. In this study, fluorinated hematite was used for the removal of U(VI) from aqueous solution in batch system. Pseudo-first order and pseudo-second order models were used for analyzing kinetics of batch technique.

1.6   MOTIVATION OF PRESENT WORK

Hematite has been investigated for several reasons and applications. There is lot of impetus in improving its properties by structural modification (nano hematite), variation in morphology and by doping. Although various elements doping into hematite and composite of hematite have been prepared for getting desired properties. However, the surface fluorination of of hematite has not yet explored. The surface fluorination of TiO_2 is reported in literature for improving photocatalytic activity [Park and Choi, 2004]. It was thought appropriate that the similar approach of surface fluorination may be applied for improving the photocatalytic, magnetic and adsorption characteristics of hematite.

1.6.1 Introduction of surface fluorination

Surface fluorination is a ligand exchange between surface hydroxyl groups on Metal oxide and fluoride anions

$$\equiv M^* - OH + F^- \longleftrightarrow \equiv M^* - F + OH^-$$
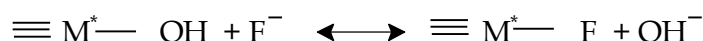
Where, M is metal ion.

1.6.2 Advantages of surface fluorination

- Surface fluorination is reported to increase surface electric conductivity and charge density.
- Transport of electron and hole occurs through surface. Hence surface property will have significant impact on any electrochemical process.
- The recombination rate of photogenerated electrons and holes can greatly reduce by F^- ions due to their strong electro-negativity, as indicated in Figure 1.8. Actually, F^- ion acts as electron-trapping sites on the surface to trap the photogenerated electrons.
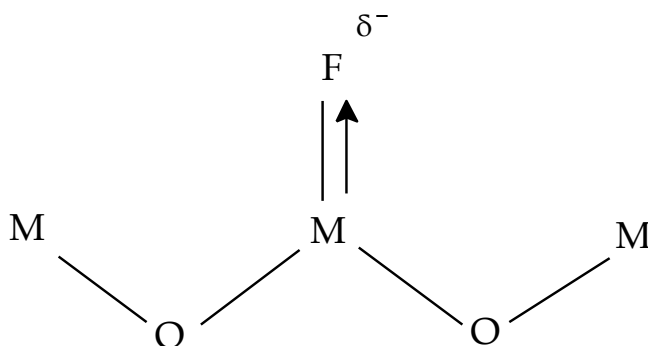

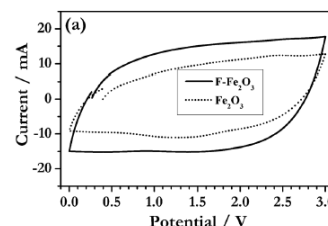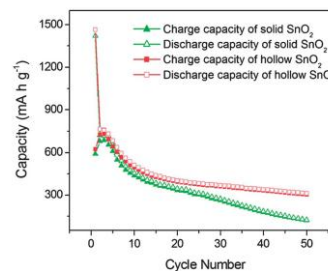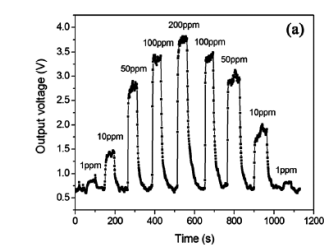Figure 1.8: Surface fluorinated structure

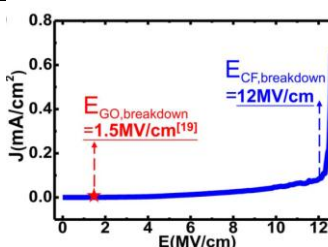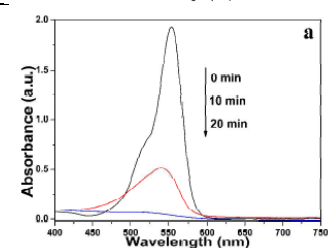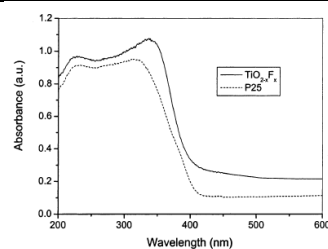- Surface fluorination alters surface charges and hence can change magnetic and adsorption characteristics of material

1.6.3 Advancements in fluorinated materials and their application

Several materials such as TiO_2, SnO_2, graphene and iron oxide have been fluorinated for improving their catalytic activity. The literature survey of fluorinated materials, describing their achievements, is presented in table 1.7.

Table 1.7: Fluorinated material and their applications

SNo	Material	Achievement		Reference
1.	F-TiO$_2$ powder: preferred Anatase phase. It was prepared by reacting Sodium fluoride (NaF) with aqueous TiO$_2$ suspensions	Significant enhancement on photo-catalytic activity		[Park and Choi, 2004]
2.	Fluorinated SnO$_2$. It was prepared by dissolving stannous fluoride (SnF$_2$) and adipic acid and reaction was conducted at 180°C for 6 h using Teflon lined stainless steel autoclave	Faster RhB dye degradation		[Wang et al., 2015]
3.	Fluorination of Graphene. It was carried out in Plasma-enhanced chemical vapor deposition (PECVD) chamber using graphene (deposited on Cu foil via CVD) and CF$_4$ gas	Achieved more than 10 MVcm$^-$ breakdown electric field which is the highest value for dielectric materials in 5 nm thickness		[Ho et al., 2014]
4.	Fluorinated TiO$_2$ nano sheets loaded with 2 wt. % Pt. TiO$_2$ nano sheets were fabricated by reacting mixed solution of HF and tetrabutyl titanate in hydrothermal vessel	Obtained much higher photo-catalytic activity (169.1, µmol h$^-$) than Degussa P25 TiO$_2$ (133.6 µmol h$^-$)		[Yu et al., 2010]
5.	Fluorinated hierarchical SnO$_2$ hollow spheres. The sample was prepared in water via hydrothermal method using SnCl$_4$.5H$_2$O, as the source of tin and NaF/ NH$_4$F as morphology controlling agent	Hierarchical SnO$_2$ hollow spheres demonstrated better charge-discharge capacity than SnO$_2$ solid spheres. The cyclic performance was also better for Hierarchical SnO$_2$		[Wang et al., 2012]
6.	Fluorine doped Fe$_2$O$_3$ prepared by microwave irradiation (700 W) using iron nitrate and NH$_4$F	Enhanced pseudo-capacitive performance compared with that of pristine hematite due to availability of better current collector		[Karthike yan et al., 2014]

7.	Fluorine doped Fe_2O_3 (Fe_2O_{3-x} F_x). It was synthesized using $FeCl_3 \cdot 6H_2O$, KCl, NH_4F and urea in DI water and ethanol medium using stainless steel autoclave (Teflon-lined) at 180 °C for 12 h	Enhanced lithium storage capacity as the accelerated Li ions solvation/desolvation processes benefit from fluorination		[Wang et al., 2017]
8.	Surface fluorinated TiO_2 was prepared by soaking TiO_2 coated glass plate in NaF solution for 30 min	Achieved faster kinetics of photo chemical oxidation (PCO) of gaseous acetaldehyde on $F-TiO_2$ than that on bare TiO_2		[Kim and Choi, 2007]
9.	Surface fluorinated TiO_2 nano sheets prepared by $Ti(OC_4H_9)_4$ and 40 wt. % HF in a desiccated Teflon-lined autoclave at ambient temperature	Attained better photocatalytic activity than Degussa P-25 TiO_2 and pristine TiO2 nanoparticles owing to synergistic effect of surface fluorination and exposed (001) facets		[Yu et al., 2010]
10.	Defect enriched iron fluoride oxide nano porous film (IFONFs) prepared by partial conversion of the nano-porous Fe-oxide using F_2 gas, produced by NH_4F	Hetero-catalysts efficiently catalyze water splitting in alkaline electrolyte with significant stability due to substantial contribution of surface/edge defects		[Fan et al., 2018]
11.	Iron oxy-fluoride prepared by surface fluorination of nm sized Fe_3O_4 and F_2 gas fluidized bed reactor at ~ 100 °C	Reported improved electrochemical performance and enhanced intercalation capacity and intercalation voltage plateau. It was attributed to the formation of surface oxyfluoride phase which has more ionicity of Fe–F bonds as compared to Fe–O		[H Zhou et al., 2013]

Therefore, the literature survey of surface fluorination reveals the enhancement in desired catalytic applications. In addition to metal oxide precursor, the fluorinating agents also plays crucial role for surface fluorination reaction. A safe, efficient and cost effective methodology is always desired for the same. Various types of fluorinating agents are mentioned in literature. The summary of fluorinating agents, their properties and physical state is presented in table 1.8.

Table 1.8: Fluorinating agents

S. No.	Fluorinating agent	Physical State & Properties	Reference
1	F_2	Gas Highly toxic, Strong oxidant and Explosive tendency Reactive for elctophilic fluorination Reaction Temp is 420 °C for metal oxides	[Tanuma et al., 2010]
2	NH_4F	Solid Reactor Preheating required at 300 °C	[Sophronov et al., 2016]
3	NaF	Poor reagent for Fluorination	[Tullock and Coffman, 1960]
4	HF	Liquid Highly corrosive, Toxic and penetrates skin faster than H_2SO_4	[Scientific, Rev 4.0]
5	DAST, Et_2NSF_3	Oily liquid corrosive, flammable, converts into explosives at > 50 °C, Reacts with water	[Nyffeler et al., 2004]
6	Selectfluor	Solid Safe, Stable, easy to handle and Reactive for electrophilic fluorination, Soluble in water and Reaction possible at room temperature	[Banks et al., 1996]

1.7 SCOPE OF THESIS WORK

From the forgoing discussion it is concluded that the hematite is a potential material to be employed in several applications. Hematite has been used in pure (bulk and nano) as well as in combination with other material to get the desired properties. Through literature survey, surface fluorination is also an important treatment of material to get improved performance. Surface fluorination of hematite can be carried out using various fluorinating agents. F-TEDA is reported as safe and effective fluorinating agent and therefore, has been chosen for fluorination. In this study, surface fluorination of hematite using several fluorinating agents has been attempted.

The main objectives of present thesis are given as under:
- Synthesis and physical characterization (and electrochemical) of surface fluorinated hematite.
- Electrochemical characterization of material and evaluation for PEC water splitting & DSSC application.
- Measurement of magnetic properties and application as microwave absorber
- Application of surface fluorinated hematite for uranium removal from waste water

1.8 CLOSING REMARK

This chapter presented an overview on hematite, its applications and properties along with demerits. Detailed literature survey for surface fluorination using various fluorinating agents and catalysts are presented. Three potential applications of surface fluorinated hematite, viz. photoelectrochemical water splitting, radar absorption and uranium removal from waste water are elaborated in subsequent chapters of present thesis.